

Drivers for mass and momentum exchange between the main channel and river bank lateral cavities

Ouro, Pablo; Juez, Carmelo; Franca, Mário

DOI

[10.1016/j.advwatres.2020.103511](https://doi.org/10.1016/j.advwatres.2020.103511)

Publication date

2020

Document Version

Accepted author manuscript

Published in

Advances in Water Resources

Citation (APA)

Ouro, P., Juez, C., & Franca, M. (2020). Drivers for mass and momentum exchange between the main channel and river bank lateral cavities. *Advances in Water Resources*, 137, Article 103511. <https://doi.org/10.1016/j.advwatres.2020.103511>

Important note

To cite this publication, please use the final published version (if applicable). Please check the document version above.

Copyright

Other than for strictly personal use, it is not permitted to download, forward or distribute the text or part of it, without the consent of the author(s) and/or copyright holder(s), unless the work is under an open content license such as Creative Commons.

Takedown policy

Please contact us and provide details if you believe this document breaches copyrights. We will remove access to the work immediately and investigate your claim.

Drivers for mass and momentum exchange between the main channel and river bank lateral cavities

Pablo Ouro^{a,*}, Carmelo Juez^b, Mário Franca^{c,d}

^a*Hydro-environmental Research Centre, School of Engineering, Cardiff University. The Parade CF24 3AA, Cardiff, United Kingdom.*

^b*Instituto Pirenaico de Ecología, Consejo Superior de Investigaciones Científicas (IPE-CSIC), Campus de Aula Dei, Avenida Montañana 1005, 50059 Zaragoza, Spain.*

^c*River Basin Development chair group, IHE-Delft Institute for Water Education, Delft, The Netherlands.*

^d*Department of Hydraulic Engineering, Delft University of Technology, Delft, The Netherlands.*

Abstract

Large-Eddy Simulations (LES) are used to investigate the governing processes involved in mass and momentum transfer between the flow in the main channel and symmetrically-distributed lateral bank cavities. In-cavity free-surface velocities, based on laboratory measurements made in an open channel, are used to validate the numerical results. A main vortical structure dominates the in-cavity flow which, despite the shallow nature of the flow, features a remarked three dimensional dynamics. LES results outline the largest velocities through the mouth of the cavity are attained in two thin regions near the bottom-bed and free-surface. In the shear layers established between the main channel and cavities is where the main transfer of turbulent momentum is made between these two flow regions, and the numerical simulations capture well the instantaneous coherent flow structures, e.g. Kelvin-Helmholtz vortices. LES captures a low-frequency standing wave phenomenon even with a rigid-lid approximation adopted at the free-surface boundary. Momentum exchange between cavities and main channel is analysed using the Reynolds Averaged momentum equation in the transverse direction, revealing that the pressure gradient term is the unique contribu-

*Corresponding author

Email addresses: ourop@cardiff.ac.uk (Pablo Ouro), carmelo.juez@ipe.csic.es (Carmelo Juez), m.franca@un-ihe.org (Mário Franca)

Preprint submitted to Advances in Water Resources

December 5, 2019

tor to flushing momentum out of the cavities whilst convection and Reynolds normal stress terms are responsible for its entraining into the cavity. Furthermore, sediment deposition areas documented in the laboratory experiments are linked with the simulated hydrodynamics, which correlate with regions of low turbulent kinetic energy and vertical velocities near the bottom of the channel. Overall, the results shed new light into the complex mechanisms involved in mass and momentum transfer; this will aid to design embayments more efficiently regarding sediment transport processes.

Keywords: Large-Eddy Simulation, Turbulence, Open channel flow, Mass transport, Hydrodynamics, River bank embayments

1 Introduction

Lateral embayments or cavities are often present in natural or human-influenced rivers. In natural rivers these typically constitute areas of sediment accumulation and flow velocity diversity, making these areas ecology hotspots within the fluvial network and controls of the river basin distribution of water and sediments. Artificial lateral cavities or local widening are often implemented in channelised rivers as nature-inspired river restoration measures. Anthropologically altered rivers have typically uniform cross sections and monotonous river banks, which contrast with natural river channels where large-scale and diversified flow and morphology can be found. This hinders the development of fish and vegetation habitats that require areas with differentiated flow velocities (Wood and Armitage [1], Kemp et al. [2]). With the intention to foster new flow patterns that diversify the velocity fields and promote the accumulation of sediment and sheltering conditions for aquatic biota, local widening establishing lateral embayments or cavities is a common practice in restoration projects mimicking natural conditions. The so-called Wandos in Japan are built to enable areas for fish spawning and nursery (Uno et al. [3], Nezu and Onitsuka [4]) and Ribi et al. [5] showed the suitability of lateral embayments to provide shelter to fish. Harbors in rivers may be conceptualised as cavities lateral to the flow in the main channel, and these may be subjected to siltation of material transported in the main stream (Langendoen et al. [6], van Schijndel and Kranenburg [7]). Finally, lateral embayments may be artificially created to capture fine sediments and thus maintain a central navigable channel, as in the historical case of the *casiers de Girardon* in the lower-Rhône (France) (Thorel et al. [8]).

26 The design of the geometry of such local widenings in a river
27 reach needs to be thorough in terms of their impact on the channel
28 hydrodynamics Valentine and Wood [9], Uijttewaal et al. [10], Weit-
29 brecht et al. [11], Lesack and Marsh [12], Sukhodolov [13], Akutina
30 [14], Mignot et al. [15], Navas-Montilla et al. [16]) and on the
31 transport of such environmental variables as fine sediments (Juez
32 et al. [17, 18]), pollutants, oxygen and nutrients (Jackson et al.
33 [19, 20], Sanjou et al. [21]). As a result, numerous field, laboratory and
34 numerical studies were carried out to elucidate the mass and momentum
35 exchange mechanisms between the main flow and the lateral cavities.

36 Traditionally, it has been common to derive mass and momentum fluxes
37 from the flow patterns observed on the water surface of laboratory experi-
38 ments and in the field. However, this approach based on the superficial flow
39 features over-simplifies the complexity of these flows and ignore the possible
40 three-dimensional (3D) nature of the exchange processes observed in the in-
41 teraction between the main flow and lateral embayments. Conceived from the
42 existing knowledge in the literature, Figure 1 presents a conceptual model of
43 open-channel flow when lateral embayments perpendicular to the main flow
44 are present, which includes: a main recirculating vortex inside the cavity
45 occupying most of its volume; vertically-oriented coherent structures which
46 are shed from the shear layer with a frequency f_{SL} ; secondary low-energetic
47 vortices in the internal corners of the cavity; and standing resonant waves
48 that appear due to the enclosed water domain (also called seiches, Kimura
49 and Hosoda [22]) oscillating at a frequency f_{SW} in the cross-flow direction
50 and causing important pressure fluctuations.

51 Transport and settling of sediments in open channel flow can vary de-
52 pending on the flow conditions, cross-section, channel aspect ratio or physical
53 properties of the sediments, among others. Nikora and Goring [23] evidenced
54 that turbulence is a key factor in sediment transport flux, which is often ne-
55 glected and sediment flux is often associated solely to the mean flow, and
56 that phenomena such as turbulent bursting events are well correlated in time
57 with sediment transport processes. A larger degree of complexity arises in
58 curved channels or when lateral embayments perpendicular to the main flow
59 are found.

60 Juez et al. [17] carried out systematic laboratory experiments in an open
61 channel, with a large number of different geometries of lateral embayments in
62 the channel banks, to investigate the interplay between flow hydrodynamics
63 and the transport (under suspension) and accumulation of fine sediments.

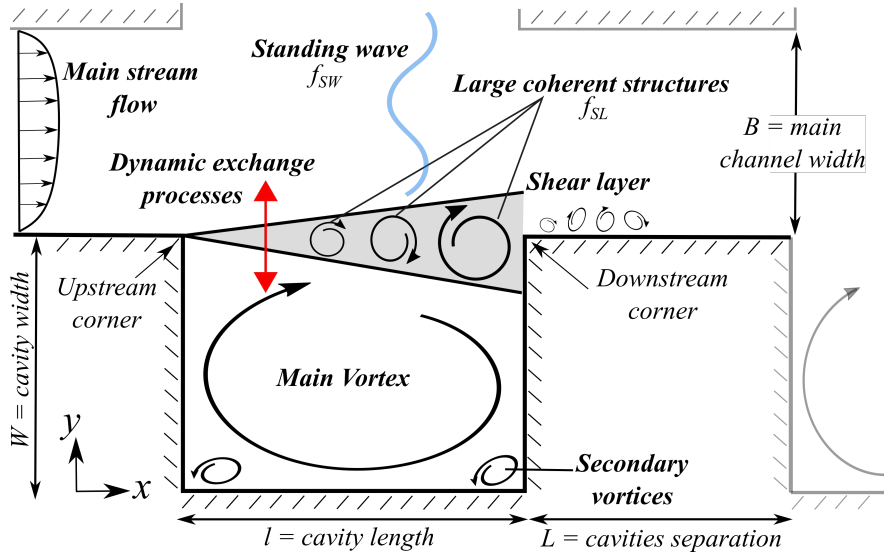


Figure 1: Schematic of the flow phenomena typically present in the hydrodynamics of lateral bank cavities. The lateral cavities are characterised by the cavity length l , the distance between two cavities L and the lateral width of the cavities W .

64 The in-cavity sedimentation pattern for several combinations of geometrical
 65 configurations and flow conditions were analysed under a two-dimensional
 66 framework. However, the results pointed out the existence of 3D flow fea-
 67 tures which relate the location and magnitude of the in-cavity flow patterns
 68 with sedimentation patterns and amount of fine sediment trapped. In their
 69 studies, Juez et al. [17, 24] observed evidences that the three-dimensionality
 70 of the flow was non-negligible, especially for the less shallow flow conditions,
 71 which did not allow to fully elucidate the direct link between the flow and
 72 the sediment transport processes.

73 To unravel the details of such complex flow, high-fidelity detailed numeri-
 74 cal simulation tools were used. Both Detached-Eddy Simulations (DES) and
 75 Large-Eddy Simulations (LES) are techniques that aid to understand the
 76 hydrodynamics of multi-scale turbulent flow structures under the presence
 77 of groynes and lateral embayments (McCoy et al. [25], Constantinescu et al.
 78 [26], Fang et al. [27]). These computational approaches, if equipped with the
 79 necessary high spatial resolution, can accurately resolve the dominant quasi-
 80 2D flow structures, e.g. large-scale energetic or shear-layer vortices, and also
 81 smaller 3D vortices. DES or LES not just provide the required resolution of
 82 the turbulent structures but they can accurately predict areas of flow sep-

83 aration of high importance in open channel and river flows, proving their
84 superiority to Reynolds Averaged Navier-Stokes (RANS) computations (van
85 Balen et al. [28], Juez et al. [29], Navas-Montilla and Murillo [30]). Thus,
86 these eddy-resolving techniques provide valuable and complete information
87 of the turbulent flow dynamics (Ouro et al. [31]), which ultimately, govern
88 mass and momentum exchange processes (McCoy et al. [32], Gualtieri [33]).

89 By means of LES, the turbulent 3D flow hydrodynamics are investigated
90 and the drivers of mass and momentum processes between the main chan-
91 nel and lateral embayments determined. Ultimately, these are related to the
92 sediment erosion/transport processes observed in the laboratory experiments
93 by Juez et al. [24]. Furthermore, the identification of preferential regions for
94 mass and momentum transfer across the opening of the cavities is possible
95 through the results of the numerical simulations. This is essential informa-
96 tion in what concerns the design of lateral embayments either to function
97 as river restoration measures, as fluvial harbours or as sediment traps to
98 keep main channels navigable. The present study focuses on one geometrical
99 configuration experimentally tested in Juez et al. [17] with three different
100 flow discharges. This geometrical configuration was chosen from others pre-
101 viously investigated, since it corresponded to sedimentation patterns which
102 contained flow diversity and morphology, hence ideal as nature-inspired so-
103 lution for river restoration. The numerical simulations herein outlined adopt
104 the large-eddy simulation approach to resolve the governing equations using
105 the in-house code Hydro3D (Ouro et al. [34]). Despite these large-eddy sim-
106 ulations do not consider the sediment transport, the hydrodynamic results
107 serve as a proxy to link the flow fluxes to the observed sediment transport
108 pathways.

109 **2. Laboratory experiments and numerical simulations**

110 *2.1. Laboratory setup*

111 Experiments were carried out in a channel which works in a closed circuit
112 with the following components (see Juez et al. [17, 18] for a more detailed
113 description): (i) an upstream 2 m long, 1 m wide and 1 m high tank for mixing
114 suspended sediments, (ii) a rectangular 7.5 m long, 1.0 m wide and 1.0 m high
115 open-channel with 0.1% slope, and (iii) a downstream tank of 3.5 m long, 1
116 m wide and 1 m high that collects the water and sediments for recirculation.
117 The water is pumped from the downstream to the upstream tank through a
118 pipe system equipped with a valve to control the discharge and a flow meter.

119 The channel bottom is smooth and made of painted wood. **Upstream, the**
 120 **transition between the head tank and the channel reach is made**
 121 **by a honeycomb-type flow tranquilliser.** **Downstream from the**
 122 **channel, a Venetian gate allows the flow depth to be controlled.**
 123 The base channel banks were modified by placing concrete bricks by the
 124 lateral walls. This allowed to build lateral embayments in the laboratory
 125 channel (see Figure 2).

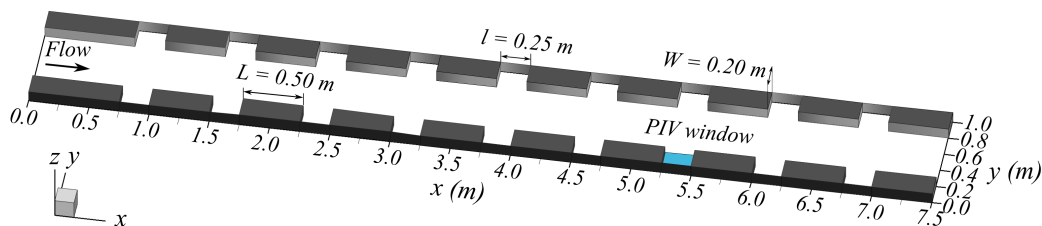


Figure 2: Representation of the channel configuration tested in Juez et al. [17], including the relevant geometric dimensions. The cavity in which PIV measurements were taken is highlighted in blue.

126 Two-dimensional (2D) surface velocity fields in the lateral embayments
 127 were measured by means of surface PIV technique. Therefore, instantaneous
 128 (u, v) , mean (U, V) and fluctuating (u', v') values for the streamwise and
 129 spanwise velocities were recorded at the water surface. The water level was
 130 recorded all through the experiments by an ultrasonic probe.

131 Uniform fine sediment with a $d_{50} = 0.2$ mm was supplied in the upstream
 132 tank of the channel at the beginning of each test. The mean diameter of the
 133 fine sediment particles was representative of the Rhône river (Federal Office
 134 of Environment [35]). Sediments were trapped inside the lateral cavities.
 135 At the end of the experiments, the sediment deposits inside the cavities
 136 were photographed. The obtained photos were treated to determine the area
 137 occupied by the settled sediments.

138 The lateral embayments configuration studied in this work corresponds to
 139 geometrical configuration 2.1 in Juez et al. [17], i.e. 0.25 m long (l) and 0.20 m
 140 wide (W) cavities with a streamwise spacing between consecutive cavities (L)
 141 of 0.40 m. The main channel width (B) is 0.60 m. Three different discharges
 142 were tested experimentally, which correspond to different values of the ratio
 143 between the water height, h , and the channel width, b : $b/h = 17.26 - 7.20$;
 144 i.e. from more to less shallow uniform flow conditions. Table 1 displays
 145 the main flow characteristics of the experiments herein studied, namely flow

146 discharge (Q), water depth (h), bulk velocity (U_0), bulk Reynolds number
 147 ($Re = hU_0/\nu$, where ν is the water kinematic viscosity), and Froude number
 148 ($Fr = U_0/(gh)^{1/2}$, where g stands for the gravity acceleration).

Case	Q [L/s]	h [m]	U_0 [m/s]	Re [-]	Fr [-]
Q1	4.8	0.035	0.227	28,487	0.39
Q2	8.5	0.050	0.295	50,568	0.42
Q3	15.0	0.070	0.355	80,645	0.43

Table 1: Hydrodynamic conditions of the configurations studied.

149 2.2. Numerical framework

150 High-fidelity numerical simulations are performed using the in-house code
 151 Hydro3D (Ouro et al. [36]), which resolves the flow dynamics by means of
 152 Large-Eddy Simulation (LES) (Liu et al. [37], Ouro et al. [31, 38], Stoesser
 153 [39], Stoesser et al. [40]). In the framework of LES, the flow structures
 154 larger than a given filter size, e.g. grid spacing, are explicitly resolved whilst
 155 those smaller are modelled (Rodi et al. [41]). Hence, the governing equations
 156 in LES are the spatially-filtered mass and momentum conservation Navier-
 157 Stokes equations for incompressible viscous flow that read as:

$$\frac{\partial u_i}{\partial x_i} = 0 \quad (1)$$

$$\frac{\partial u_i}{\partial t} = -\frac{1}{\rho} \frac{\partial p}{\partial x_i} - \frac{\partial u_i u_j}{\partial x_i} + \nu \frac{\partial^2 u_i}{\partial x_j^2} - \frac{\partial \tau_{ij}}{\partial x_j} + \frac{1}{\rho} \frac{\partial p_0}{\partial x_i} \delta_{11} \quad (2)$$

158 Here u_i and x_i are the vectors of velocities and coordinates, p denotes
 159 pressure, ν and ρ are the kinematic viscosity and density of the fluid respec-
 160 tively, τ_{ij} represents the sub-grid scale stresses, and δ is the Kronecker delta.
 161 Periodic streamwise flow condition (x_1) is adopted with a constant pressure
 162 gradient p_0 , which ensures uniform flow rate Q , applied only to the main
 163 channel region, i.e. not applied to the lateral cavities region (Bomminayuni
 164 and Stoesser [42]).

165 In Hydro3D, the computational domain is discretised as a rectangular
 166 Cartesian mesh divided into smaller sub-domains which are inter-communicated
 167 via Message Passing Interface (MPI) to perform the simulation in parallel

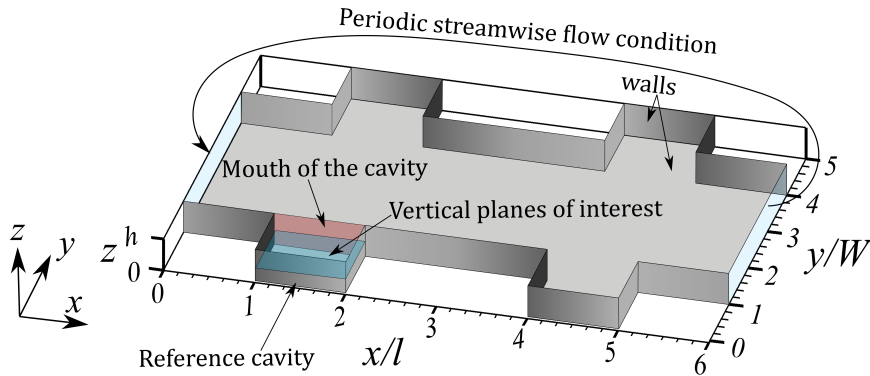


Figure 3: Geometric configuration of the computational domain which corresponds to configuration 2.1 in the laboratory work of Juez et al. [17]. Given the symmetrical and periodical characteristics of the physical system, two lateral embayments on each side were used when building the computational domain. A periodic streamwise flow condition is imposed in the main channel upstream and downstream ends.

168 (Ouro et al. [34]). Staggered storage arrangement of velocities is adopted with
 169 fourth-order central differences to approximate velocity fluxes and the Pois-
 170 son pressure equation is solved using a multi-grid technique (Cevheri et al.
 171 [43]). The simulation is advanced in time using a fractional-step method
 172 with a three-step Runge-Kutta method providing a second order accuracy
 173 in time. The Wall-Adapting Local-Eddy viscosity model from Nicoud and
 174 Ducros [44] is used to calculate the sub-grid scale stress tensor.

175 The computational domain spans 1.5 m long ($x/l = 6$) and comprises
 176 two cavities on each lateral boundary of the channel, as depicted in Figure
 177 3. The simulations start with an initial uniform velocity field and run for
 178 several flow-throughs using inflow-outflow conditions to allow the flow to
 179 develop within the cavities and remove any transients in the main channel
 180 from the initial flow state. Thereafter, periodic streamwise conditions are
 181 applied, which represents a scenario of an infinite array of lateral cavities.
 182 At the bottom and lateral walls, a non-slip condition is imposed as the first
 183 computational grid cell is within the viscous sub-layer. The free-surface is
 184 treated as a shear-free rigid lid as the Froude numbers of the studied cases
 185 are below 0.5 (Constantinescu et al. [26], Koken and Constantinescu [45]).
 186 Seiching across the channel was not observed during the experiments for the
 187 selected geometrical configuration herein chosen (Juez et al. [18]).

188 The resolution of the numerical grids is uniform across the whole domain

189 and details are provided in Table 2. For the two lowest discharges (Q1 and
 190 Q2) the grid size is 1 mm, whilst for Q3 the same resolution is used in x -
 191 and y -direction and that in the vertical increases to 0.5 mm, as the increase
 192 in friction velocity due to higher flow discharge requires higher resolution to
 193 have the first grid off the wall within the viscous sub-layer ($\Delta z^+ = \Delta z u_* / \nu <$
 194 12, Rodi et al. [41]). The meshes comprise a total of 38.5, 55 and 154 million
 195 elements for the different cases and the simulations run using between 100
 196 and 300 CPUs on *Supercomputing Wales* facilities.

Case	Δx [m]	Δz [m]	Δz^+ [-]	u_* (LES) [m/s]	u_* (Exp) [m/s]	t_e [s]
Q1	0.0010	0.0010	6.91	0.014	0.018	2.53
Q2	0.0010	0.0010	8.73	0.017	0.021	2.86
Q3	0.0010	0.0005	5.06	0.020	0.024	3.46

Table 2: Details of the grid resolution in streamwise (Δx) and vertical (Δz) directions, vertical resolution in wall units (Δz^+), friction velocity (u_*) obtained from experiments and LES, and eddy turn-over time ($t_e = h/u_*$), for the flow configurations studied.

197 For the time integration in the LESs, variable time step is adopted with
 198 constant Courant-Friedrichs-Lewy (CFL) value equal to 0.3 in order to guar-
 199 antee numerical stability. As the bulk conditions of the three study cases are
 200 different, the simulations run for an approximately equivalent physical time
 201 of 190 eddy turn-over time, defined as $t_e = h/u_*$, representative of the time-
 202 scale of the largest flow structures in the main channel. This criterion yields
 203 to a total simulation times of 559 s, 620 s and 680 s in cases Q1, Q2 and Q3,
 204 respectively. These time integration intervals are long enough to ensure con-
 205 verged flow statistics. The LES-computed friction velocity presented in Table
 206 2 is obtained from the time-averaged pressure gradient as $u_* = \sqrt{dp/dx R_h / \rho}$,
 207 where R_h stands as the main-channel hydraulic radius and dp/dx is the time-
 208 averaged pressure gradient imposed in the main channel to keep a constant
 209 flow rate Q . LES consistently underpredicts the friction velocity by approxi-
 210 mately 15% compared to the experimental value. This may be attributed to
 211 the lack of modelling the concrete rough walls or representing an infinite ar-
 212 ray of lateral embayments using periodic boundary conditions, which might
 213 lead to slightly different flow conditions from those found in the experiments
 214 at the measured location.

215 The analysis of the transport of momentum across the cavity opening is
 216 analysed using the LES results, evaluated with the contribution of each terms

217 of the Reynolds-averaged momentum equation in y -direction, in which steady
 218 conditions are assumed, i.e. $\partial V/\partial t = 0$. The adopted Reynolds-Averaged
 219 Navier-Stokes (RANS) equation in y -direction reads:

$$0 = \underbrace{-U \frac{\partial V}{\partial x}}_{\text{I}} - \underbrace{V \frac{\partial V}{\partial y}}_{\text{II}} - \underbrace{W \frac{\partial V}{\partial z}}_{\text{III}} - \underbrace{\frac{\partial u'v'}{\partial x}}_{\text{IV}} - \underbrace{\frac{\partial v'v'}{\partial y}}_{\text{V}} - \underbrace{\frac{\partial v'w'}{\partial z}}_{\text{VI}} - \underbrace{\frac{1}{\rho} \frac{\partial P}{\partial y}}_{\text{VII}} + \underbrace{\nu \left(\frac{\partial^2 U}{\partial x^2} + \frac{\partial^2 V}{\partial y^2} + \frac{\partial^2 W}{\partial z^2} \right)}_{\text{VIII}} \quad (3)$$

220 **Here the terms I, II and III represent the convective transport**
 221 **of y-axis momentum**, the momentum transport due to turbulent stresses
 222 correspond to the terms IV to VI, term VII is the pressure gradient that
 223 drives the flow into the cavity, and term VIII corresponds to the viscous
 224 stresses.

225 3. Results

226 3.1. Time-averaged flow

227 Time-averaged flow field developed in the reference cavity and in the
 228 adjacent area of the main channel is presented in Figure 4 for the horizontal
 229 plane at $z/h = 0.5$. Contours of mean streamwise (a) and transverse (b)
 230 velocities, streamwise (c) and transverse (d) turbulence intensities, Reynolds
 231 shear stress $u'v'$ (e) and turbulent kinetic energy (defined as $tke = u_i u_i / 2$)
 232 (f), are shown for the flow conditions corresponding to case Q2. Results are
 233 adimensionalised using the bulk velocity of the main channel, U_0 , and shear
 234 velocity, u_* .

235 Flow streamlines reveal that a single recirculating vortex (hereinafter de-
 236 noted as Main Vortex (MV)) is formed within each cavity occupying most
 237 of its volume governing the in-cavity flow, whilst secondary vortical struc-
 238 tures of much smaller size are generated at the corners, forced by continuity
 239 and the no-slip condition at the cavity walls. These can be deemed to have
 240 negligible influence on the hydrodynamics (Mignot et al. [15]). Maximum
 241 streamwise negative velocities are found near the wall opposite to the cavity
 242 opening, reaching values up to $U \approx -0.25U_0$. The in-cavity flow observed
 243 corresponds to the skimming flow type due to its geometric aspect ratio near
 244 the unity (Meile et al. [46]). In such flow type, the recirculating MV is
 245 largely decoupled from the main stream flow and no interference between

246 cavities happens, which can be translated into reduced mass and momentum
 247 exchange. Furthermore, typically if the aspect ratio is from 0.5 to
 248 1.5, one single eddy is observed in the cavity.

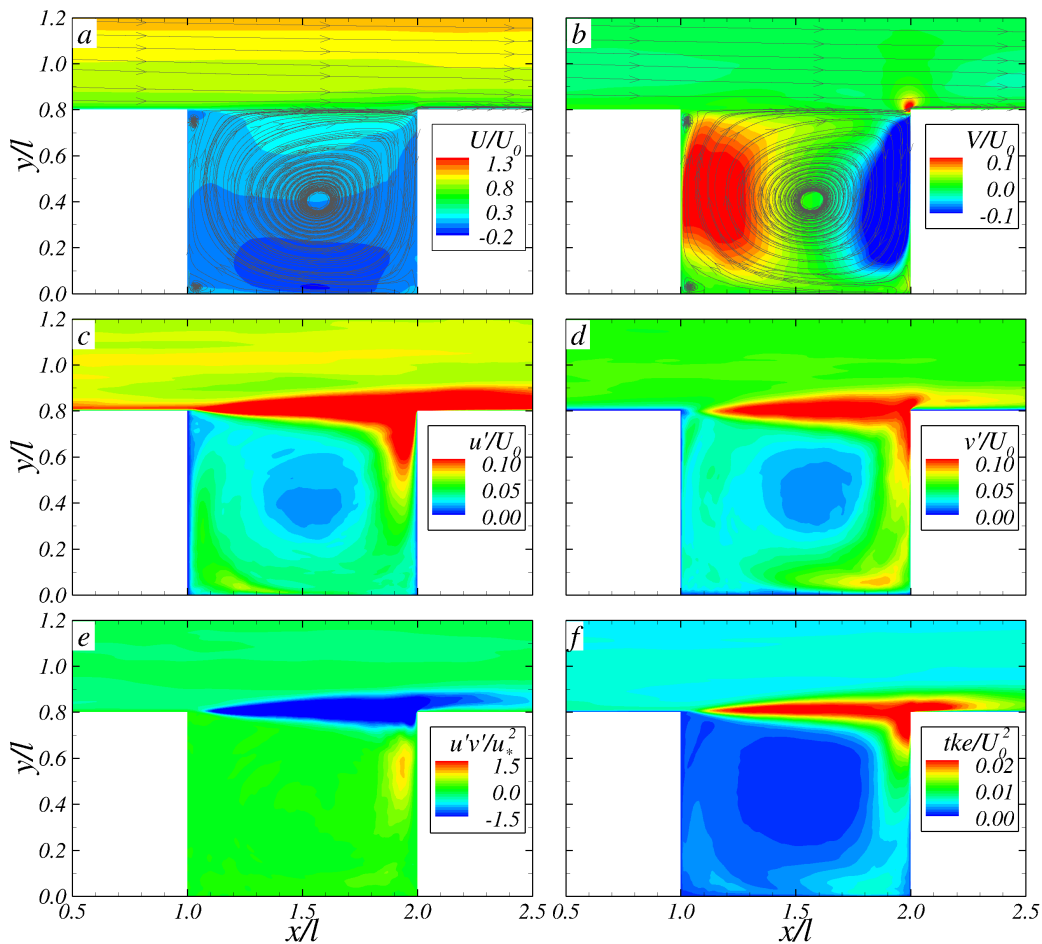


Figure 4: Distribution of normalised time-averaged (a) streamwise (U/U_0) and (b) transverse velocities (V/U_0), (c) streamwise (u'/U_0) and (d) transverse (v'/U_0) turbulence intensities, (e) Reynolds shear stress ($u'v'/u_*^2$), and (f) turbulence kinetic energy (tke/U_0^2), for the case Q2 and for the horizontal plane at $z/h = 0.5$. Flow streamlines are only drawn in a and b for sake of simplicity.

249 Areas of large velocity fluctuations reveal high turbulence activity and
 250 second-order statistics are observed to be maximum across the shear layer
 251 generated between the cavities and the main channel, i.e. $y/l = 0.8$, with
 252 nevertheless some degree of penetration into the cavity near the downstream

253 inner wall. In the contribution to turbulent kinetic energy, u' values are
 254 found larger than v' across the mouth of the cavity even though momentum
 255 exchange between main stream and cavities seems to be predominantly in
 256 the transverse direction. Regions of large u' are also observed across the
 257 main channel lateral wall at downstream of the cavities. These fluctuation
 258 of streamwise velocities are due to the coherent structures recurrently shed
 259 in the shear-layer as depicted in Figure 1 and presented later in Section 3.2.
 260 Inside the cavity, minima of the velocity fluctuations are attained close to
 261 the core of the recirculating MV suggesting that this is mostly stationary in
 262 time without major spatial oscillations across the cavity region, as commonly
 263 found in skimming flows (Weitbrecht et al. [11]). Contours of Reynolds shear
 264 stress reveal the shear layer grows in size since the upstream outer corner and
 265 reaches its widest distribution close to the downstream cavity corner (Mignot
 266 et al. [15]).

267 A key aspect in the simulation of embayment flows is the prediction of
 268 the position of the core of the recirculating main vortex, MV, since this is
 269 somewhat related to the sedimentation patterns which are observed in the
 270 cavity bottom. Figure 5 presents the relative coordinates $(x/l, y/W)$ of the
 271 recirculating vortex core for two extreme positions in the water column, i.e.
 272 water surface ($z = h$) and cavity bottom ($z = 0$). These positions were
 273 determined based on the streamlines of mean flow from LES (e.g. Figure
 274 4a). In the same figure, the position of the MV core for the surface observa-
 275 tions made in the experimental work with surface PIV (Juez et al. [17]) are
 276 represented as well.

277 The 3D nature of this vortical structure is obvious confirming the results
 278 by Tuna et al. [47]: the superficial position of the main vortex does not match
 279 the position of the core of the vortex close to the bottom. Taking into account
 280 the vertical variation, for case Q1, the shift in the core position is small. On
 281 the contrary, for the two higher discharges and water depths (Q2 and Q3),
 282 the vortex centre moves towards the mouth of the cavity with increasing
 283 submergence. The largest change in the core position is observed for the
 284 highest Reynolds number case, i.e. Q3. A trend with the flow is observed
 285 for both the numerical and laboratory results: when becoming shallower, the
 286 core of the vortical structure approaches the cavity entrance. Overall, a good
 287 agreement is found between computational and experimental data, with the
 288 LES predicting the x -locations within a 4% error margin and within a 10%
 289 accuracy for y -coordinates.

290 The distribution of the mean flow across the transition plane between the

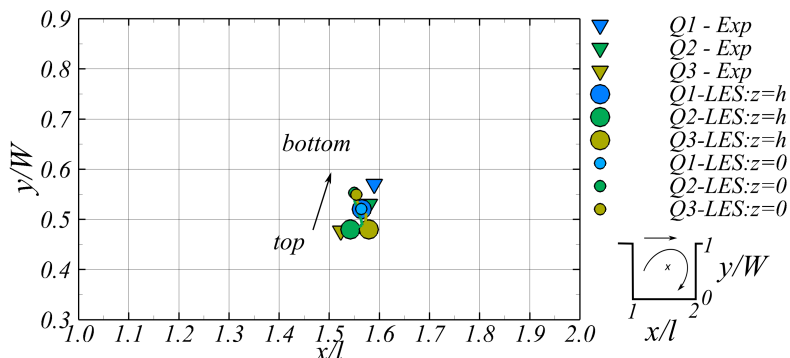


Figure 5: Location of the recirculating main vortex core position obtained from time-averaged velocities computed with LES and experimental measurements from Juez et al. [17].

291 main stream and the lateral cavity is presented in Figure 6 for the three cases
 292 withh contours of streamwise and transverse velocities. A similar pattern
 293 of U/U_0 is developed in cases Q2 and Q3, in which the largest velocities
 294 are found in the downstream half with maximum values attained near the
 295 bottom and at the free-surface. In case Q1 there seems to exist a more
 296 uniform distribution of the maximum velocity through the channel-cavity
 297 transitions section, which is a consequence of shallowness.

298 The spacial region of maximum negative cross-flow velocities V/U_0 ap-
 299 pears to be similar among cases, specifically at $1.2 < x/l < 1.9$, at $z/h \approx 0.3$
 300 for Q2 and Q3, whilst for Q1 a slightly higher position is found of $z/h \approx 0.4$.
 301 The cross-flow mean velocity V here measured is the main responsible for
 302 exchange of mass and momentum between the cavities and the main channel
 303 by the mean flow. The negative V -velocity areas identify where mass entrains
 304 into the cavity (Sanjou and Nezu [48]). Conversely, mass flush out mainly
 305 occurs at two locations, across the entire water depth near the downstream
 306 cavity wall at $x/l > 1.9$ and, with lower velocity values, between $0.2 < z/h <$
 307 0.9 in the upstream half of the cavity mouth section. Note that for cases Q2
 308 and Q3, in the region of $1.8 < x/l < 1.9$, entraining flow is found across the
 309 water column while this is not observed in the case with the lowest discharge.

310 Figure 7 shows second-order flow statistics, only for case Q2 for the sake
 311 of brevity. The mostly 2D distribution of the three components of turbu-
 312 lence intensity and the turbulent kinetic energy reveal that the flow near
 313 the upstream corner of the cavity is less turbulent while, after a distance
 314 of $x/l = 1.2$, the turbulence activity in this pane grows. Lower levels of

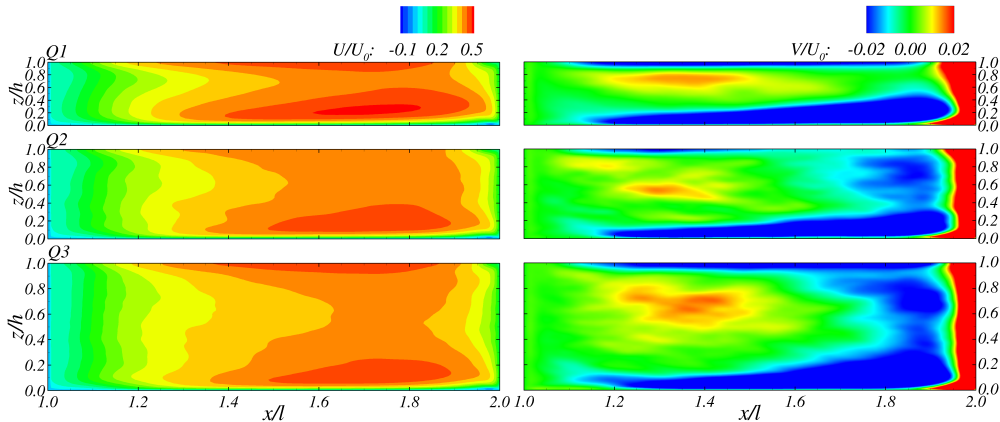


Figure 6: Distribution at a plane through the mouth of the cavity at $y/W = 1.0$ (cf. Figure 3) of the normalised time-averaged streamwise (U/U_0) and transverse (V/U_0) velocities for the three cases.

315 turbulence are observed near the channel bed and free-surfaces. Contours
 316 of Reynolds shear stresses $u'v'$ along the mouth of the cavity feature neg-
 317 ative values with an almost uniform distribution in the vertical direction.
 318 The growing turbulence activity from the upstream towards the downstream
 319 cavity wall is in agreement with the development of the shear layer sketched
 320 in Figure 1 and visible in Figure 4, which is the expected main region of
 321 turbulence production in this flow.

322 Qualitative comparison of velocities at the free-surface layer between LES
 323 and experiments is presented in Figure 8, with profiles of U/U_0 and V/U_0
 324 along transverse locations $x/l = 1.25$ and 1.50 for the three cases. Distribu-
 325 tion of U shows that negative velocities are found for $y/W < 0.5$ for most
 326 cases, as expected from the contours of U in Figure 4a. **While in the mid**
 327 **region of the cavity LES agrees well with the PIV data, discrepan-**
 328 **cies are observed near the wall opposite to the mouth of the cavity,**
 329 **i.e. $y/W = 0.0$. This is attributed to the known difficulty for the 2D-**
 330 **PIV to provide accurate velocity estimates near the walls, due to**
 331 **the decreasing concentration of tracer particles and the strong flow**
 332 **gradients near the walls, these velocity measurements are usually**
 333 **biased (Kähler et al. [49]).** Profiles of transverse velocity show never-
 334 theless a good match between computational and experimental data at both
 335 locations for all the studied cases.

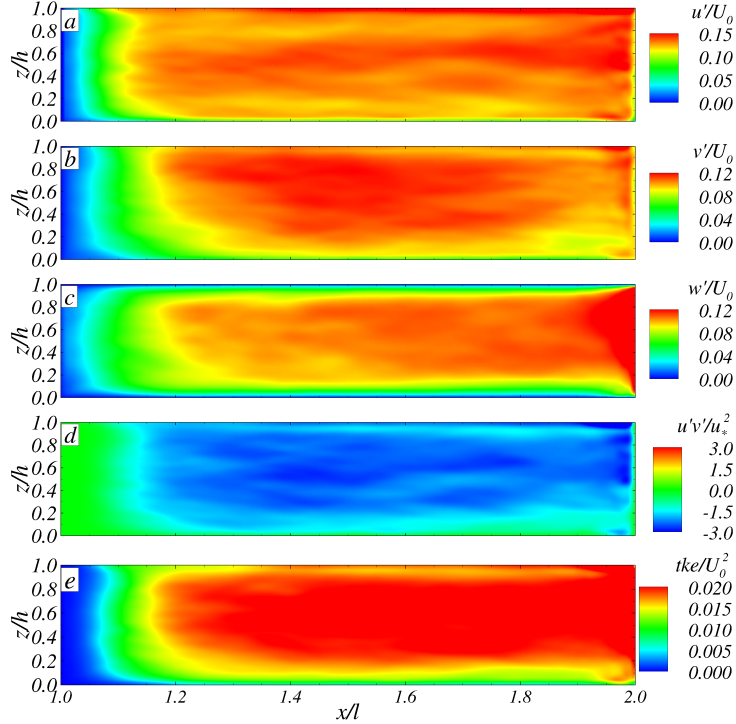


Figure 7: Distribution at a plane through the mouth of the cavity at $y/W = 1.0$ (cf. Figure 3) of the (a) streamwise (u'/U_0), (b) transverse (v'/U_0) and (c) vertical (w'/U_0) turbulence intensities, (d) Reynolds shear stress ($u'v'/u_*^2$) and (e) tke/U_0^2 , for the case Q2.

336 3.2. Instantaneous turbulent flow structures

337 The turbulent mechanisms of mass and momentum exchange between
 338 the main channel and the lateral cavities are conditioned by the coherent
 339 structures which form in the shear layer and penetrate inside the cavities.

340 Figure 9 presents the turbulent structures deduced with iso-surfaces of
 341 instantaneous pressure fluctuation, $p' = p - P$, and coloured with streamwise
 342 velocity for half of the channel width for the case Q2. A broad spectrum
 343 of flow structures travelling through the main channel is observed with the
 344 largest ones advected along the middle of the main channel cross-section.
 345 Closer to the side walls the size of the turbulent structures reduces notably.
 346 Of great interest are the Kelvin-Helmholtz (KH) vortices developed in the
 347 shear layer at the mouth of the cavities as a consequence of the velocity dif-
 348 ference between the low-velocity cavity flow and higher-velocities in the main
 349 stream. In their inherent 3D shape, KH vortices appear to keep a fairly co-

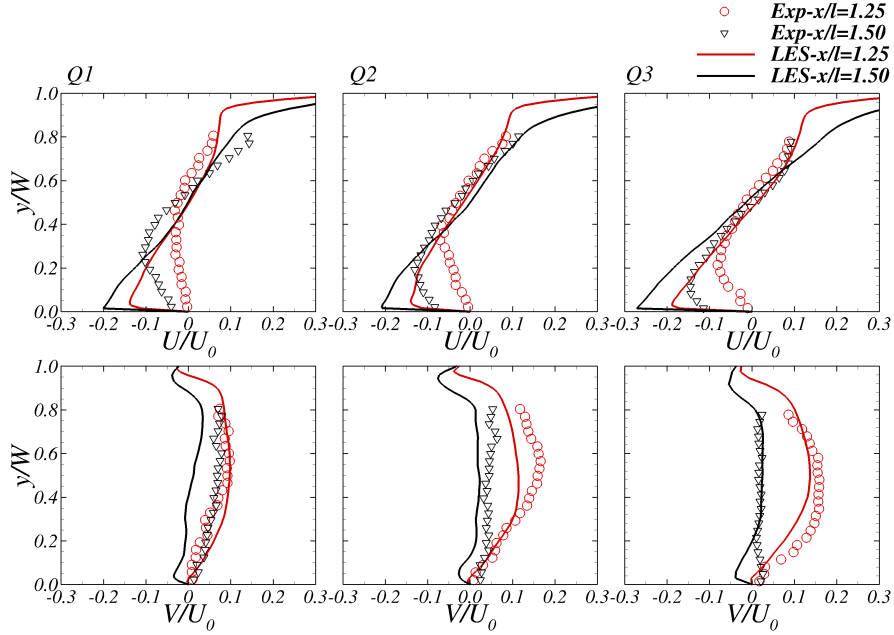


Figure 8: Transverse profiles of streamwise (U/U_0) and transversal (V/U_0) velocities at $x/l = 1.25$ and 1.50 . Comparison between experiments (Juez et al. [17]) and present LES results.

350 herent vertical structure across the water depth while convected downstream,
 351 as no large velocity gradients in the vertical direction are observed (Mignot
 352 et al. [50]). Such coherent shape is more consistent for case Q1 as the flow is
 353 shallower. Furthermore, the large-scale MVs occupy the entire embayments
 354 volume with vertically-evolving loci at relatively similar position over the
 355 cavity cross-section, as depicted in time-averaged streamlines in Figure 4.

356 At the internal cavity corners secondary recirculating vortices are ob-
 357 served, which, as previously mentioned, are forced by continuity and by the
 358 shear between the MVs and sidewalls. Note that their size is considerably
 359 smaller than the MVs and, consequently, their influence in the hydrodynam-
 360 ics of the in-cavity flow, and the processes of exchange of mass and momen-
 361 tum between the cavity and the mains channel which are here under analysis,
 362 can be deemed negligible (Weitbrecht et al. [11]).

363 Figure 10 displays contours of instantaneous pressure, p , with vectors of
 364 2D velocities with magnitudes $(0.2 \cdot u, v, 0)$ at a plane located at $z/h = 0.5$
 365 for the flow conditions corresponding to the highest discharge, Q3, with a

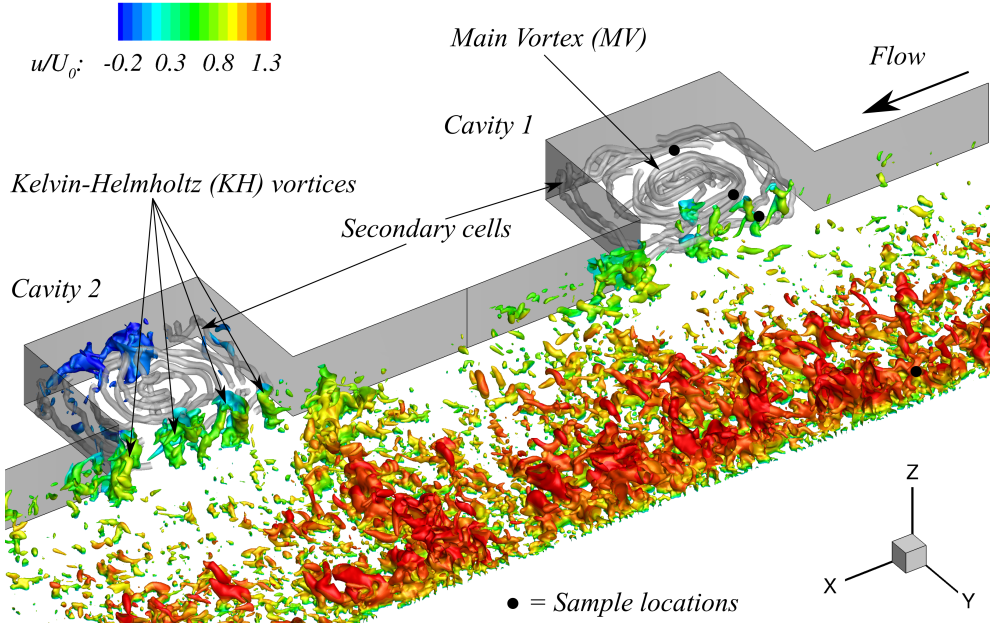


Figure 9: Instantaneous flow structures represented with iso-surfaces of pressure fluctuation p' coloured with normalised streamwise velocity for the case Q2. Only half of the channel width is displayed.

366 time lapse of 0.40 s between each consecutive snapshots. Here the two points
 367 located at $x/l = 1.5$ at $y/W = 0.875$ and 1.125 are included as they are used
 368 to collect pressure signal time series for the shear layer instability analysis in
 369 the spectral domain. At the upstream corner at $t = t_0$, the onset of the shear
 370 layer instabilities occurs as a result of the velocity gradients between regions
 371 (Mignot et al. [50]). In their early formation stages, the Kelvin-Helmholtz
 372 (KH) structures are relatively small but, as they are convected downstream,
 373 grow in size due to the interaction with the ambient flow and travel with
 374 an almost parallel direction to the cavity mouth transverse plane. For this
 375 reference cavity on the right-hand side of the main channel, KH vortices
 376 feature a clockwise rotation as a consequence of them being fed at their
 377 front edge by transversal velocities from the main channel moving into the
 378 cavity and at their trailing edge by those velocities being flushed out from the
 379 cavity. During the last stages of their downstream advection, KH vortices
 380 progressively loss coherence until impinging the downstream cavity corner,
 381 when they partially entrain into the cavity or continues with the main stream
 382 (Rockwell and Knisely [51]). This is the main process of turbulent transport

383 scalars between the cavity and the main channel, as previously reported in
 384 Mignot et al. [15] for square-like single cavity flows.

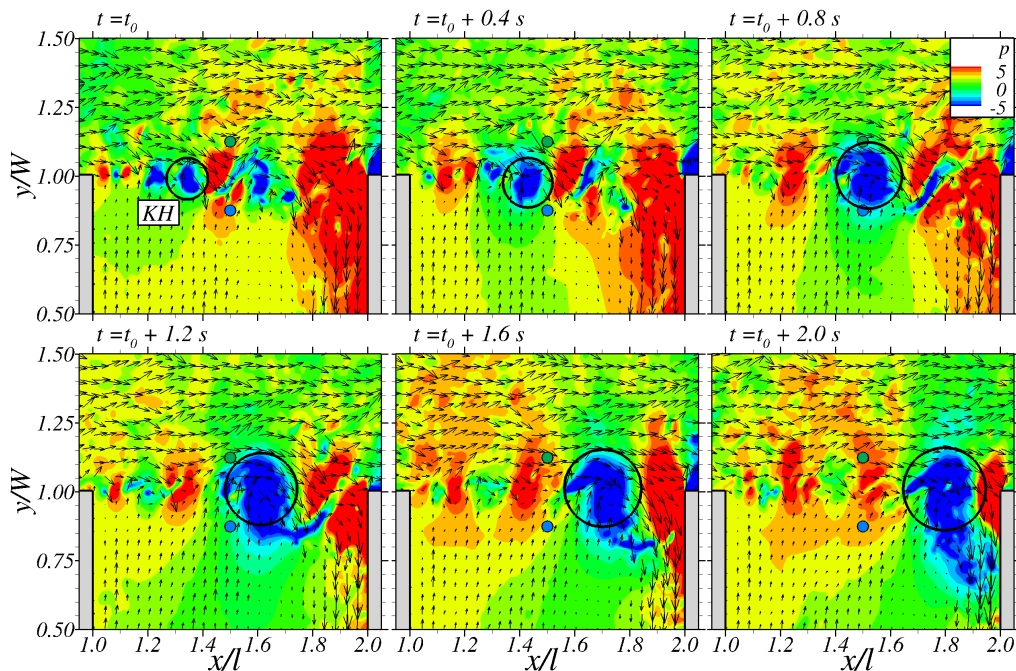


Figure 10: Contours of instantaneous pressure, p , with velocity vectors of components $(0.2 \cdot u, v, 0)$ at a plane located at $z/h = 0.5$ for the flow conditions corresponding to the highest discharge, case Q3. The snapshots have a time lapse of 0.40 s among them.

385 3.3. Spectral analysis of the variations in the pressure field

386 The results on the pressure field measured within the flow can reveal
 387 whether standing wave (SW) phenomena occur and whether there is a co-
 388 herent pattern in the temporal generation of KH vortices travelling across
 389 the shear layer. As found in Wölfinger et al. [52], when the frequency of the
 390 standing wave, f_{SW} and that of the shear-layer vortex shedding f_{SL} coincide,
 391 a lock-on phenomenon is experienced. Under these resonance conditions, the
 392 hydrodynamics of the in-cavity flow can dramatically change, modifying the
 393 mass and momentum exchanges between the main channel-cavities. Juez
 394 et al. [17] showed that under such conditions the in-cavity sedimentation
 395 processes can be also completely altered. The standing waves that appear
 396 in enclosed water domains are called seiches. Whilst f_{SL} depends on the ge-
 397 ometry of the cavity and flow conditions (Wölfinger et al. [52]), f_{SW} can be

398 approximated to be the eigenfrequency of the first eigenmode of the standing
 399 wave, f_1 , determined as:

$$f_1 = \frac{\sqrt{gh}}{2B} \quad (4)$$

400 To quantify the differences in the variation of the pressure field at different
 401 locations in the transversal direction (y -direction), spectra of the pressure
 402 time-series, at the four sample locations located at $y/W = 0.125, 0.875,$
 403 1.125 and 2.500 at mid water depth and depicted in Figure 9, are computed
 404 and presented in Figure 11. These locations are aligned with the cavity
 405 centre ($x/l = 1.5$) transverse to the main flow direction, as depicted in Fig.
 406 10, allowing to determine the relevant oscillating phenomena conditioning in
 407 flow field.

408 At frequencies in inertial region and above, all the spectra feature two
 409 outstanding regions of slopes $-5/3$ and -3 . These results suggest the existence
 410 of quasi-2D vortical structures that follow an inverse turbulent energy cascade
 411 (Nikora et al. [53], Sommeria [54]): energy transfer from the small eddies
 412 towards the large vortical structures is verified. Such turbulent dynamics
 413 corresponds to those observed in Figure 10 in the shear layer region where
 414 small eddies are formed, advected downstream, and coalesce to form larger
 415 turbulent structures.

416 For high frequencies, in the region of the inverse cascade (with -3 slope)
 417 and regardless the flow conditions, the spectra at the four different transverse
 418 locations collapse with the same level of energy. However, for lower frequen-
 419 cies, the energy decay observed for the case Q1 is quite different between the
 420 points inside of the cavity, i.e. $y/W < 1.0$, and those outside. These obser-
 421 vations for Q1, when compared with the cases Q2 and Q3, suggest that there
 422 is a separation between the turbulent dynamics between the inner and outer
 423 regions of the cavity for shallower flows. At the dissipative scales, when the
 424 flow tends to isotropy, this difference is not seen anymore due to a similar
 425 spectral energy decay found in all cases.

426 Two notable peaks are always observed in the production range of the
 427 spectra presented. One corresponds to shedding frequency of the KH vortices
 428 produced in the shear layer region while a second energy peak corresponds
 429 to the standing wave. For the case Q1, one of the peaks is common to the
 430 three positions inside and the verge of the cavity: $y/W = 0.125, 0.857$ and
 431 1.125 . A second energy peak at higher frequency is observed for all the four

432 positions, including $y/W = 2.500$, at the centre of the main channel. At the
 433 latter location, a signature from the KH vortices in the pressure signal is
 434 not expected according to the pressure field observed in Fig. 10. Hence, the
 435 first peak at lower frequency (f_{SL}) is attribute to the shear layer KH vortices
 436 shedding and the second peak at higher frequency (f_{SW}) to the standing
 437 wave which should be felt in the pressure field across the channel: $f_{SL} =$
 438 0.72 Hz and $f_{SW} = 1.17$ Hz respectively, for case Q1. For the cases Q2 and
 439 Q3, values of frequencies f_{SL} and f_{SW} increase with increasing flow rate and
 440 decreasing shallowness.

441 Frequencies f_{SL} and f_{SW} computed for the different cases are summarised
 442 in Table 3 together with values of f_1 (Eq. 4). The ratio between f_{SL}/f_{SW} are
 443 lower than the unity, although approaching this value with increasing flow
 444 rate, which suggests that both unsteady phenomena are not coupled, similar
 445 to the *pre lock-on* case in Wölfinger et al. [52]. For discharges higher than
 446 the ones tested, an interaction between the standing wave and shear-layer
 447 shedding is expected.

448 The ratio between the standing wave frequency from the numerical simu-
 449 lations (f_{SW}) with the theoretical standing-wave value (f_1) are close or above
 450 four, indicating that for all the studied cases no amplification of the effect
 451 of the standing wave due to resonance is expected, i.e. when $f_{SW} \approx f_1$.
 452 These results are confirmed with the lack of seiching observed during the
 453 experiments reported in Juez et al. [18].

454 Finally, in Table 3 values of the reduced velocity, defined with the bulk
 455 velocity and main channel width as $U_r = U_0/(f_1 B)$, for the three cases
 456 Q1, Q2 and Q3 are presented. As U_r is lower than the unity which again
 457 indicates that non-resonance conditions are expected. In the experimental
 458 work by Wölfinger et al. [52], for a single lateral cavity with similar Reynolds,
 459 Froude numbers and reduced frequency, analogous *pre lock-on* transient flow
 460 behaviour was found.

461 Four ranges can be identified in the spectral distribution of the pressure
 462 signal, as depicted in Figure 12 for Q2 at two sample locations, one inside the
 463 cavity and another in the main channel centreline. At the lowest frequencies,
 464 typically larger than the shear-layer shedding frequency, the energy produc-
 465 tion range "I" is found. The range "II" is characterised by an energy decay
 466 that follows a -1 slope, which was not drawn in Figure 11 for clarity purposes.
 467 Nikora [55] linked the -1 slope to the superposition of vortical structures in
 468 the energy cascade process. It is in this spectrum interval in which energy
 469 peaks at f_{SL} and f_{SW} are found. In the inertial sub-range "III", the energy

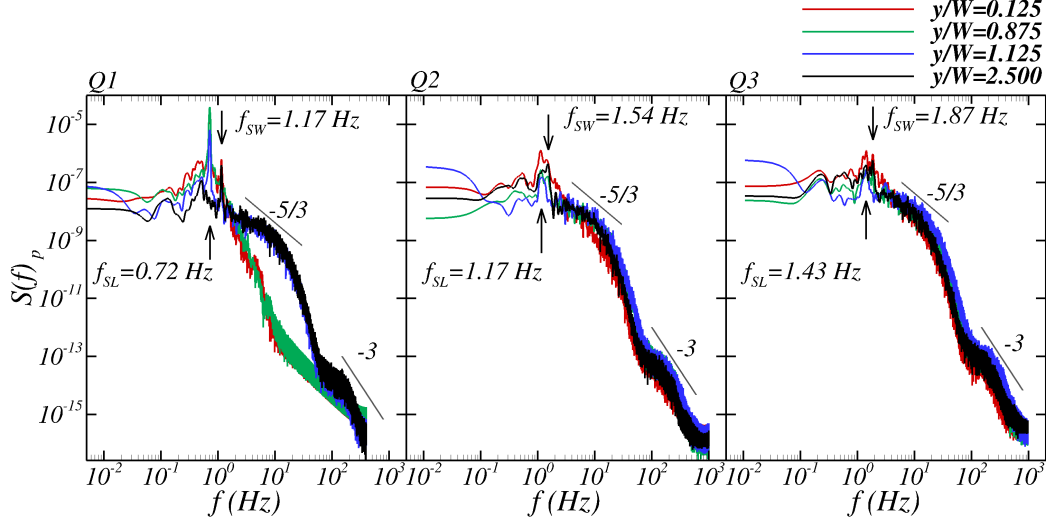


Figure 11: Power spectral density computed from pressure time-series at four spatial samples located at different transverse locations and depicted in Figure 9, for $x/l = 1.5$ and $z/h = 0.5$ (see Figure 9) and for all the studied cases Q1, Q2 and Q3.

Case	h [m]	f_{SW} [Hz]	f_{SL} [Hz]	f_1 [Hz]	f_{SL}/f_{SW} [-]	f_{SW}/f_1 [-]	U_r [m/s]
Q1	0.035	1.17	0.72	0.29	0.61	3.99	0.76
Q2	0.050	1.54	1.17	0.35	0.76	4.40	0.84
Q3	0.070	1.87	1.43	0.41	0.77	4.51	0.86

Table 3: Values of water depth, frequencies of shear layer vortex shedding (f_{SL}), standing wave (f_{SW}), approximated standing wave (f_1) and their ratio and reduced velocity (U_r) for the three cases. Values of the frequency of the shear layer (f_{SL}) and standing wave (f_{SW}) were obtained through the signal analysis displayed in Figure 11. The value of the approximated standing wave (f_1) was computed by means of Eq. 4.

470 decay follows the $-5/3$ slope as previously shown in Figure 11. At frequencies
 471 in the order of 10^2 Hz the dissipation range "IV" takes place, which features a
 472 -3 slope owed to the inverse cascade process commonly found in shallow flows.
 473 Kraichnan [56] justified that both $-5/3$ and -3 slopes can be simultaneously
 474 present in the energy spectrum of two-dimensional flows, being the former
 475 a consequence of the largest flow scales transferring kinetic energy from low
 476 to high frequencies, whilst the latter is due to the small scales feeding the
 477 larger ones.

478 The intrinsic high-resolution of the simulations is evidenced thanks to

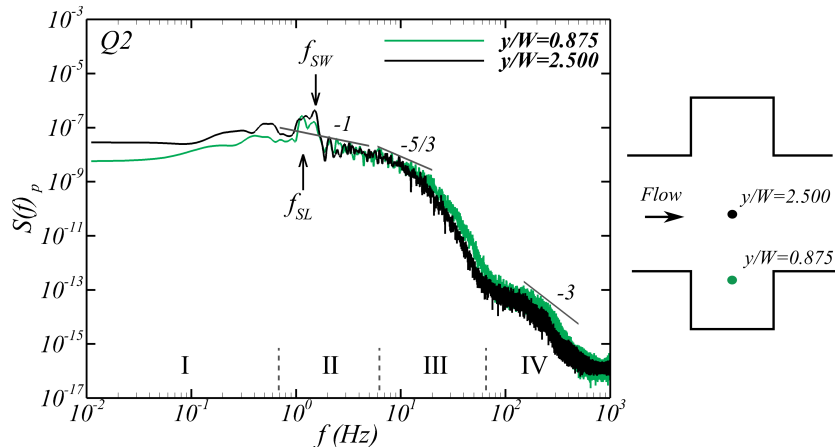


Figure 12: Identification of the main ranges and slopes found in power spectral density computed from pressure time-series. Samples are located inside ($y/W = 0.875$) and outside ($y/W = 2.5$) of the cavity at $x/l = 1.5$ and $z/h = 0.5$, for the case Q2.

479 the full palette of frequencies resolved. It is noteworthy that the present
 480 LES capture remarkably well the presence of the standing wave effect in the
 481 pressure field, despite adopting a rigid-lid approximation without explicitly
 482 resolving the free-surface motion. The sub-grid scale (sgs) model, responsible
 483 for taking into account the flow scales lower than the grid resolution, does
 484 not introduce any additional dissipation until frequencies in the order of 10^3
 485 Hz. This small interplay of the sgs model is also quantified with the ratio of
 486 the sgs to kinematic viscosity, which attains values lower than the unity in
 487 most of the computational domain.

488 3.4. Momentum transfer between main channel and lateral cavities

489 Governing processes in the momentum transfer between the main channel
 490 and lateral cavities are analysed looking at the components of the Reynolds
 491 Averaged Navier-Stokes (RANS) momentum equation in the spanwise direc-
 492 tion (y -RANS), defined in Eq. 3. The embayments under analysis have a
 493 high aspect ratio, which means that the flow is expected to be of the skim-
 494 ming type as described in Meile et al. [46]. **The aspect ratio corresponds**
 495 **to the case of the so-called "closed" cavity in Meile et al. [46].** Un-
 496 der this scenario, the entrainment of main-channel streamwise momentum is
 497 limited, in opposition to what occurs in lower-aspect ratio geometries, i.e.
 498 with relatively larger cavity opening length.

499 The scale over which the terms in y -RANS equation are time-averaged is
500 sufficiently large to ensure statistically convergence of second-order moments.
501 This means that the instantaneous flow structures developed in the shear
502 layer, said to be responsible for mass and momentum exchange (Weitbrecht
503 et al. [11], Constantinescu et al. [26]), are accounted within the turbulent
504 stresses of the flow. Cross-sectional mean values of the y -RANS equation
505 are integrated over the mouth of the cavity plane are shown in Figure 13 for
506 the three cases normalised by l/U_0^2 . Positive values indicate flushing out of
507 momentum whilst negative denote its entrainment into the cavity.

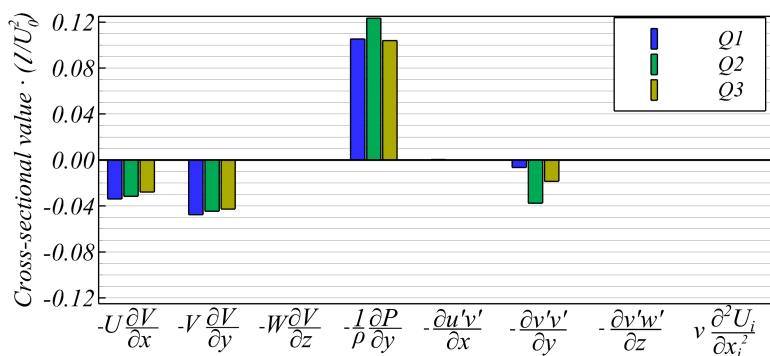


Figure 13: Components of the terms of the y -RANS equation, spatially averaged over the mouth of the cavity plane, for the three cases Q1, Q2 and Q3.

508 The results show that the pressure gradient is the only term responsible
509 for driving the momentum out the cavity into the main channel. On the
510 other hand, terms involved in the entrainment of momentum from the main
511 channel to the cavity are mainly the convection terms $U \partial V / \partial x$ and $V \partial V / \partial y$
512 and, to a lesser extent, the $v'v'$ Reynolds stress. The gradient of the tur-
513 bulent momentum flux $u'v'$ has a negligible contribution to the transverse
514 momentum exchange so does the viscous terms, as expected due to the high
515 Reynolds number of the flow.

516 There is a similar pattern in the y -RANS results integrated over the
517 mouth of the cavity for the three flow conditions. However, in the case Q2,
518 there is a larger contribution from the pressure gradient counterbalanced
519 by an additional larger gradient of turbulent flux $v'v'$, being the convection
520 terms of the mean flow field very similar to those in Q1 and Q3. These
521 results imply that the momentum exchange mechanisms vary depending on
522 the flow conditions for the same cavity configuration. This agrees with the

523 results on the sediment trapping efficiency obtained in the experimental work
524 by Juez et al. [17]. In their case, for the present high-aspect ratio geometry,
525 the maximum efficiency was attained for Q2 and close values were obtained
526 for Q1 and Q3, indicating a clear relation between momentum and sediment
527 exchanges between the main channel and the cavities.

528 The distribution of the four main terms from the y -RANS equation across
529 the mouth of the cavity is presented in Figure 14 for the case Q2. It is
530 observed that the convective term $U\partial V/\partial x$ aids to momentum entrainment
531 (negative values) in the 20% downstream part of the cavity whilst positive
532 values are mostly found between $1.5 < x/l < 1.8$. The term $V\partial V/\partial y$ features
533 only two region of large positive values, namely near the channel bottom and
534 free-surface, indicating the regions where momentum is transported from the
535 cavity to the main channel.

536 Near the downstream wall, the convective terms corresponding to the
537 mean flow have large negative values contribute all in the same direction
538 of transverse momentum entrainment. The turbulent stress term, together
539 with the convective ones, contribute to the net transport of spanwise mo-
540 mentum from the main channel into the cavity, and this is well-observed in
541 its distribution over the mouth of the cavity which exhibits mostly negative
542 values.

543 Finally, the pressure gradient contours in Figure 14 show its positive
544 contribution counterbalancing the turbulent term in the region $0.1 < x/l <$
545 0.5 , and between $0.85 < x/l < 1.0$ the convective terms.

546 3.5. Mass exchange

547 Exchange of mass processes between the high-momentum main channel
548 and lateral embayments vary depending on the geometric characteristics of
549 the cavity. **The present cavities feature an aspect ratio W/l equal to**
550 **0.8 (i.e. skimming flow type) implying there is no deflection from**
551 **the main channel flow into the cavity.** The exchange velocity E across
552 the channel-cavity interface is defined as the cross-sectional average value of
553 the absolute transverse velocity, and the exchange coefficient k relates the
554 former exchange velocity with the bulk velocity, which read as:

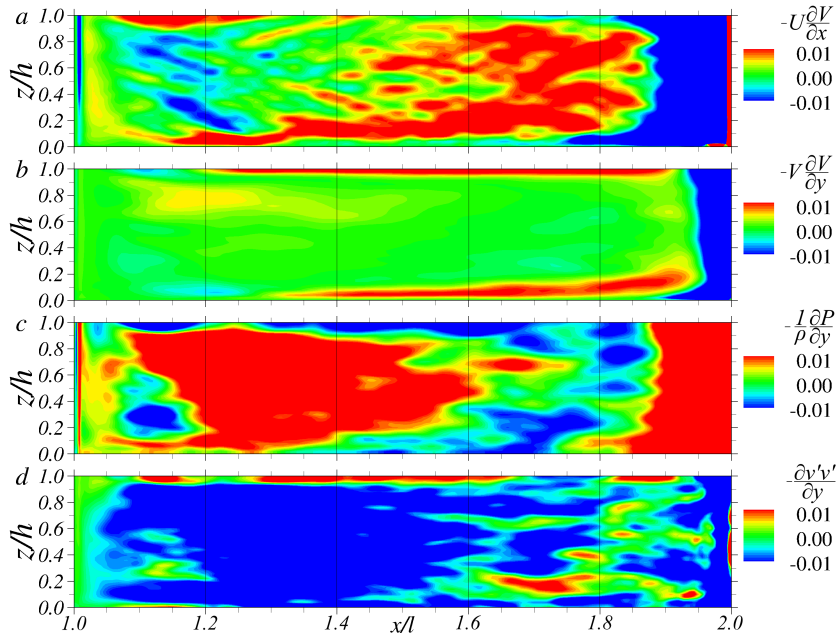


Figure 14: Distribution along the cavity mouth of the main y -RANS equation components for the Q2 case.

$$E = \frac{1}{Wl} \int_0^l \int_0^W |V| dz dx \quad (5)$$

$$k = \frac{E}{2U_0} \quad (6)$$

555 Table 4 presents the exchange coefficient values, k , obtained in the ex-
 556 periments of Juez et al. [18], those computed from the LES integrated across
 557 the mouth of the cavity at $y/W = 1.0$ (see Fig 6), and also those obtained
 558 from LES using the values of $|V|$ at the domain top lid. The latter values
 559 are calculated similarly to the experimental entrainment coefficients which
 560 were obtained by using PIV measurements at the water surface. The ex-
 561 perimental and numerical entrainment coefficients differ notably, and only
 562 the k values at LES-top display values with the same order of magnitude
 563 as the ones displayed in the laboratory. Disparity in the results of k be-
 564 tween experiments and numerical predictions have previously been reported
 565 (Constantinescu et al. [26]). **Furthermore, k values obtained with PIV**

566 decreases when the flow discharge is increased (from Q1 to Q3).
 567 This agrees with Mignot et al. [15] but not with the results re-
 568 ported in Weitbrecht et al. [11]. However, in Weitbrecht et al. [11]
 569 the seiching phenomenon was not observed. Regarding the magni-
 570 tude of the values, k (PIV) and k (LES-top) display similar values
 571 to those obtained in Weitbrecht et al. [11], Mignot et al. [15].

Case	k (PIV)	k (LES)	k (LES-top)
Q1	0.043	0.0081	0.0145
Q2	0.029	0.0090	0.0140
Q3	0.015	0.0084	0.0147

Table 4: Values of the dimensionless exchange coefficient obtained during the experiments of Juez et al. [18] using PIV, and computed with LES using velocities across the cavity-opening plane and those at the free-surface.

572 Despite the shallow nature of the flow, the turbulent structures that de-
 573 veloped in the shear layer display 3D turbulent characteristics. Figure 9
 574 presents the turbulent structures plotted with iso-surfaces of pressure fluctu-
 575 ation. The turbulent structures in the vicinity of the shear layer are mainly
 576 contained within the main channel. The observed 3D turbulent structures
 577 behave as a vertical barrier avoiding the in-cavity development of the shear
 578 layer (McCoy et al. [25]). This is an important observation, since the mass
 579 exchange of fine sediments, pollutants or nutrients between the main chan-
 580 nel and the cavities is thus notably limited/governed by the production of
 581 turbulence in this region of the channel.

582 During the experimental campaign carried out in Juez et al. [17] plane
 583 view photos of the in-cavity sedimentation patterns were taken at the end of
 584 the experiment. These photos were treated to extract the surface occupied
 585 by the sediments. Figure 15 presents iso-surfaces of time-averaged vertical
 586 velocities $W/U_0 = \pm 0.1$, contours of turbulent kinetic energy (tke) at $z/h =$
 587 0.01, and the areas corresponding to where the sediments settled at the end
 588 of the experiments. Sediment deposition areas mostly coincide with those
 589 lacking large vertical velocities implying that near-bed vertical velocities are
 590 responsible for keeping them in suspension. Negative iso-surfaces of W are
 591 found close to the lateral walls whilst positive values are mainly in the inner
 592 recirculation area. Additionally, deposition areas also seem to correlate with
 593 those where turbulent kinetic energy values are also small. These results
 594 indicate that sediment particles are able to settle when vertical velocities

595 and turbulence are very low.

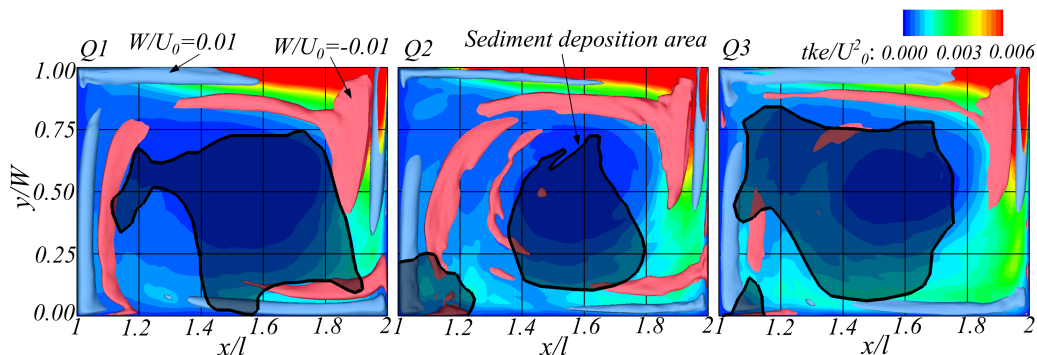


Figure 15: Comparison of the sediment deposition regions (shaded areas) obtained during the experimental campaign (Juez et al. [17]) with the computed flow field near the bottom bed of the cavity. Contours of turbulent kinetic energy are at $z/h = 0.01$ and iso-surfaces of vertical velocities show values $W/U_0 = \pm 0.1$. Note that only velocity iso-surfaces at $z = 7$ mm and below are shown.

596 4. Discussion

597 The current research adopted high-resolution LES to identify and display
 598 the major role played by the vortical structures characteristic of in-cavity
 599 flows, specifically: vertically-oriented vortical elements generated in the shear
 600 layer; a main recirculating in-cavity vortex; and small-scale in-cavity vortices.
 601 Results of the hydrodynamics revealed that the flow within the cavities are
 602 reasonably shallow with their flow dynamics largely dominated by a large-
 603 scale structure, named as Main Vortex (MV), which extends over most of
 604 this confined region. The appearance of a single MV is due to the relatively
 605 squared shape of the cavities, resembling to a skimming flow type in which the
 606 entrainment of momentum from the main stream into the macro-roughness
 607 elements is reduced. While this energetic flow structure is expected to feature
 608 a quasi-2D shape owed to the shallow flow conditions, the vertical position
 609 of its core is proven to vary with depth, especially for the deeper case. It is
 610 closer to the opening of the cavities near the bottom, whilst moving towards
 611 to the opposite wall at the free-surface.

612 The velocity differences in the transition between the high-momentum
 613 main channel and low-velocity cavities leads to the formation of shear lay-
 614 ers, in which a train of coherent vortices develops due to Kelvin-Helmholtz

615 (KH) instability. In spite of the shallow nature of the flow, these structures
616 feature a 3D nature occupying the whole water column (see Figure 9). These
617 KH vortices are relatively small structures compared to the MV and, dur-
618 ing their convection, increase in size remaining coherent until impinging the
619 downstream cavity wall, as observed in Figures 9 and 10. The KH vortices
620 travel over the mouth of the cavity plane affecting both the in-cavity flow
621 and the adjacent main channel region. A fairly uniform distribution of the
622 Reynolds stresses over the whole water depth and across the channel-cavity
623 transition is also observed due to this coherence. At the last stage, when im-
624 pinging the downstream corner of the cavity, the Kelvin-Helmholtz vortices
625 breakdown, partially entraining into the cavity or going away with the main
626 stream.

627 As a result of this activity and dominance of the KH vortices, the mass
628 exchange between the main stream and in-cavity flow is limited and, con-
629 sequently, the dimensionless exchange coefficients computed with LES are
630 lower than the ones obtained with the surface PIV (see Table 4). As shown
631 in Fig. 6, the largest transverse velocities across the mouth of the cavity are
632 found in mainly two pockets extending across most of the streamwise length
633 of the embayment but confined at vertical locations near the free-surface and
634 bottom bed. Such velocity distribution highlights that the mass exchange
635 between the main channel and cavities is largely heterogeneous. Hence, it is
636 therefore inaccurate to assume that the flow patterns observed at the water
637 surface can precisely determine the mass exchange between the main flow
638 and lateral embayments.

639 The present large-eddy simulations are able to capture temporally re-
640 current oscillations in the pressure fluctuations across the entire channel,
641 despite a shear-free rigid-lid condition is imposed at the free-surface. At
642 several sample locations distributed across the channel width, a peak in the
643 spectral energy distribution of the pressure signal is observed at frequencies
644 close to those of the theoretical standing wave. In addition, spectra inside
645 of the cavity revealed that shear-layer phenomena affect the dynamics of the
646 in-cavity flow and adjacent region of the main channel, which was observed
647 in the pathway of KH vortices during their advection in Fig. 10. The spec-
648 tral analysis also reveals that the energy of the quasi-2D MV is fed by the
649 smaller scale structures from the shear layer, observed in the -3 slope of the
650 spectra in the dissipation range. Conversely, the energy decay of the largest
651 flow structures follows a -1 slope until the inertial sub-range is reached.

652 The momentum transfer between the main channel and cavities is anal-

653 ysed with the Reynolds Averaged momentum equation in the cross-flow direc-
654 tion. The integration of each of the involved terms across the main channel-
655 cavity transition plane reveals a large impact of the pressure gradient in the
656 transverse momentum exchange. This appears to be the sole responsible
657 for the momentum flush-out from the cavities to the main stream, mostly
658 counterbalanced by the convective terms with a reduced contribution of the
659 Reynolds normal stresses. Such key role of the pressure field in the momen-
660 tum balance together with the fact that the shedding frequency of shear-layer
661 KH vortices is nearly coupled with the standing-wave frequency, can be linked
662 to the relevance of the seiche phenomenon in the sediment transport. Un-
663 der *lock-on* conditions, i.e. when the frequencies of the shear-layer vortices
664 and standing-wave matches, these phenomena intensify the changes in the
665 pressure field [52].

666 The turbulent flow characteristics computed inside the cavities served
667 as a proxy to determine the sediment exchange reported in the laboratory
668 experiments. Figure 15 displays the in-cavity sediment deposition regions
669 reported in Juez et al. [17] as well as the contours of turbulent kinetic energy
670 and iso-surfaces of mean vertical velocities near the cavity bottom. The
671 predicted patterns of iso-surfaces of vertical velocities are linked to pathways
672 of sediment movement: the sediment deposition areas are bounded by regions
673 in which vertical velocities are lower than 1% the bulk velocity and levels of
674 turbulence are very low. These findings reflect that the ease of the sediments
675 to deposit within the cavity relies on the secondary flow distribution and its
676 unsteadiness.

677 A key finding from this study is that low-frequency transverse pressure
678 changes arises as an essential factor in the sediment transport in river bank
679 lateral cavity flows. This variable is normally absent in experimental tests
680 with PIV or ADV and normally omitted in the analysis. Such importance be-
681 comes crucial to understand why sediment transport dynamics change when
682 seiching is present (Tuna et al. [47]). This, combined with the coupling of the
683 standing wave and shear-layer KH vortices shedding that can further amplify
684 the pressure field oscillations, determine when a given lateral embayment ge-
685 ometry performs best to trap sediments from the main channel, as previously
686 observed in experimental tests in Juez et al. [17].

687 Establishing the link between the flow and sediment transport is crucial
688 in understanding the geomorphological evolution of the lateral embayments.
689 The information related to the accurate quantification of the mass exchange
690 between the main channel and the lateral embayments may be used for the

691 application of measures against sedimentation problems or to identify the
692 magnitude and sources of pollutants, nutrients and carbon, which are fixed
693 to and conveyed with the sediment. For example, the impact of the release of
694 fine sediments by reservoir flushing operations on the in-cavity sedimentation
695 could be better assessed by knowing the interaction between the flow rates
696 and the geometry of lateral embayments. The long-term maintenance of the
697 cavities could thus be guaranteed. **Furthermore, as a future work the**
698 **extra density provided by the sediment particles in suspension will**
699 **be considered in the LES model to account for the variable bulk**
700 **density of the flow.**

701 5. Conclusions

702 The main drivers in the mass and momentum exchange between the main
703 channel and symmetrically-distributed river lateral cavity have been identi-
704 fied via large-eddy simulations (LES). Three cases with varying shallowness
705 and flow discharge were analysed for a single embayment geometry. Despite
706 the relatively shallow nature of the flow, the hydrodynamics notably changed
707 for each flow condition, all of which proved to be highly three-dimensional
708 both across the main channel, within the cavities and also in their transi-
709 tion region. In order to elucidate and quantify such complex flow nature,
710 high-resolution LES were carried out to complement the experimental ob-
711 servations so as to understand the driving mechanisms also involved in the
712 sediment transport.

713 Regarding mass exchange, this study outlines that large streamwise and
714 transversal velocities were mostly found in regions near the bottom and top
715 lids at the mouth of the cavities. A single main vortex occupied most of the
716 volume of each cavity, being the location of its core not uniformly distributed
717 over the water depth. The LESs captured the dominant Kelvin-Helmholtz
718 flow structures generated and convected over the shear layers developed in the
719 channel-cavity transition. Despite a rigid-lid was adopted to represent the
720 free-surface, LES captured well the standing wave phenomenon originated
721 from pressure field oscillations. This was identified from pressure spectra
722 at various locations across the channel width. Peaks in the spectral energy
723 due to the shear-layer vortices shedding were also observed but only at those
724 locations within or close to the lateral cavities.

725 The areas of sediment deposition obtained during a previous experimental
726 campaign agreed well with areas of low turbulence and vertical velocities pre-

727 dicted by the LES near the embayments bottom. This study quantified that
728 the gradient of pressure is the main responsible for the transport of trans-
729 verse momentum out of the cavity, counterbalanced by inwards transport due
730 to convection and Reynolds normal stresses. The identification of the main
731 mechanisms developed in the channel-cavity transition provides new insights
732 into the sediment exchange and deposition processes.

733 **Acknowledgements**

734 The authors would like to acknowledge the support of the Supercom-
735 puting Wales project, which is partially funded by the European Regional
736 Development Fund (ERDF) via the Welsh Government. Furthermore, the
737 second author, Carmelo Juez, is funded by the H2020-MSCA-IF-2018 pro-
738 gramme (Marie Skłodowska-Curie Actions) of the European Union under
739 REA grant agreement (number 834329-SEDILAND).

740 **References**

- 741 [1] P. Wood, P. Armitage, Biological effects of fine sediment in the lotic
742 environment, *Environmental Management* 21 (2) (1997) 203–217, doi:
743 10.1007/s002679900019.
- 744 [2] P. Kemp, D. Sear, A. Collins, P. Naden, I. Jones, The impacts of fine
745 sediment on riverine fish, *Hydrological Processes* 25 (2011) 1800–1821,
746 doi:10.1002/hyp.7940l.
- 747 [3] K. Uno, N. Kazuuma, G. Tsujimoto, T. Kakinoki, Trapping effect of
748 fine sediment in wand, *Journal of Japan Society of Civil Engineers, Ser.*
749 *B3 (Ocean Engineering)* 69 (2013) 922–927.
- 750 [4] I. Nezu, K. Onitsuka, PIV Measurements of side-cavity open-channel
751 flows. Wando model in rivers, *Journal of visualization* 5 (2002) 77–84.
- 752 [5] J. Ribi, J. Boillat, A. Peter, A. J. Schleiss, Attractiveness of a lat-
753 eral shelter in a channel as a refuge for juvenile brown trout during
754 hydropeaking, *Aquatic Science* 76 (2014) 572–541, doi:10.1007/s00027-
755 014-0351-x.
- 756 [6] E. Langendoen, C. Kranenburg, R. Booij, Flow patterns and exchange
757 of matter in tidal harbours, *Journal of Hydraulic Research* 32 (1994)
758 259–270.

- 759 [7] S. A. H. van Schijndel, C. Kranenburg, Reducing the siltation of a river
760 harbour, *Journal of Hydraulic Research* 36 (1998) 803–814.
- 761 [8] M. Thorel, H. Piégay, C. Barthelemy, B. Räßle, C.-R. Gruel, P. Mar-
762 monier, T. Winiarski, J.-P. Bedell, F. Arnaud, G. Roux, J. C. Stella,
763 G. Seignemartin, A. Tena-Pagan, V. Wawrzyniak, D. Roux-Michollet,
764 B. Oursel, S. Fayolle, C. Bertrand, E. Franquet, Socio-environmental im-
765 plications of process-based restoration strategies in large rivers: should
766 we remove novel ecosystems along the Rhône (France)?, *Regional En-
767 vironmental Change* 18 (7) (2018) 2019–2031, ISSN 1436-378X, doi:
768 10.1007/s10113-018-1325-7.
- 769 [9] E. M. Valentine, I. R. Wood, Experiments in longitudinal dispersion
770 with dead zones, *Journal of Hydraulic Division* 105(HY8) (1979) 999–
771 1016.
- 772 [10] W. S. J. Uijttewaal, D. Lehmann, A. van Mazijk, Exchange processes
773 between a river and its groyne fields: Model experiments, *Journal of
774 Hydraulic Engineering* 127 (11) (2001) 157–172.
- 775 [11] V. Weitbrecht, S. A. Socofolosky, G. H. Jirka, Experiments on Mass Ex-
776 change between Groin Fields and Main Stream in Rivers, *Journal of Hy-
777 draulic Engineering* 134 (2) (2008) 173–183, doi:10.1061/(ASCE)0733-
778 9429(2008)134:2(173).
- 779 [12] L. F. W. Lesack, P. Marsh, River-to-lake connectivities, water renewal,
780 and aquatic habitat diversity in the Mackenzie River Delta, *Water Re-
781 sources Research* 46 (12), doi:10.1029/2010WR009607.
- 782 [13] A. Sukhodolov, Hydrodynamics of groyne fields in a straight river reach:
783 insight from field experiments, *Journal of Hydraulic Research* 52(1)
784 (2014) 105–120, doi:10.1080/00221686.2014.880859.
- 785 [14] Y. Akutina, Experimental investigation of flow structures in a shallow
786 embayment using 3D-PTV. PhD Thesis., Ph.D. thesis, McGill Univer-
787 sity, Montréal, 2015.
- 788 [15] E. Mignot, W. Cai, J. I. Polanco, C. Escauriaza, N. Riviere, Measure-
789 ment of mass exchange processes and coefficients in a simplified open-
790 channel lateral cavity connected to a main stream, *Environmental Fluid
791 Mechanics* 17 (2017) 429–448, doi:10.1007/s10652-016-9495-7.

- 792 [16] A. Navas-Montilla, C. Juez, M. Franca, J. Murillo, Depth-averaged un-
793 steady RANS simulation of resonant shallow flows in lateral cavities
794 using augmented WENO-ADER schemes, *Journal of Computational*
795 *Physics* 395 (2019) 511–536, doi:10.1016/j.jcp.2019.06.037.
- 796 [17] C. Juez, I. Buhmann, G. Maechler, A. J. Schleiss, M. J. Franca,
797 Transport of suspended sediments under the influence of bank macro-
798 roughness, *Earth Surf. Process. Landforms* 43 (2018) 271–284, doi:
799 10.1002/esp.4243.
- 800 [18] C. Juez, M. Thalmann, A. J. Schleiss, M. J. Franca, Morphologi-
801 cal resilience to flow fluctuations of fine sediment deposits in bank
802 lateral cavities, *Advances in Water Resources* 115 (2018) 44–59, doi:
803 10.1016/j.advwatres.2018.03.004.
- 804 [19] T. R. Jackson, R. Haggerty, S. V. Apte, A. Coleman, K. J. Drost, Defin-
805 ing and measuring the mean residence time of lateral surface transient
806 storage zones in small streams, *Water Resources Research* 48 (10), doi:
807 10.1029/2012WR012096.
- 808 [20] T. R. Jackson, R. Haggerty, S. V. Apte, B. L. O’Connor, A mean
809 residence time relationship for lateral cavities in gravel-bed rivers and
810 streams: Incorporating streambed roughness and cavity shape, *Water*
811 *Resources Research* 49 (6) (2013) 3642–3650, doi:10.1002/wrcr.20272.
- 812 [21] M. Sanjou, T. Okamoto, I. Nezu, Dissolved oxygen transfer into a square
813 embayment connected to an open-channel flow, *International Journal of*
814 *Heat and Mass Transfer* 125 (2018) 1169 – 1180, ISSN 0017-9310, doi:
815 10.1016/j.ijheatmasstransfer.2018.04.107.
- 816 [22] I. Kimura, T. Hosoda, Fundamental properties of flows in open channels
817 with dead zone, *Journal of Hydraulic Engineering* 123 (2) (1997) 98–107.
- 818 [23] V. Nikora, D. Goring, Fluctuations of Suspended Sediment Concentra-
819 tion and Turbulent Sediment Fluxes in an Open-Channel Flow, *Journal*
820 *of Hydraulic Engineering* 128 (2) (2002) 214–224.
- 821 [24] C. Juez, M. H. Hassan, M. J. Franca, The Origin of Fine Sediment Deter-
822 mines the Observations of Suspended Sediment Fluxes Under Unsteady
823 Flow Conditions, *Water Resources Research* 54 (2018) 5654–5669, doi:
824 10.1029/2018WR022982.

- 825 [25] A. McCoy, G. Constantinescu, L. J. Weber, Numerical Investiga-
826 tion of Flow Hydrodynamics in a Channel with a Series of Groynes,
827 Journal of Hydraulic Engineering 134 (2) (2008) 157–172, doi:
828 10.1061/(ASCE)0733-9429.2008134:2.157.
- 829 [26] G. Constantinescu, A. Sukhodolov, A. McCoy, Mass exchange in a shal-
830 low channel flow with a series of groynes: LES study and comparison
831 with laboratory and field experiments, Environmental Fluid Mechanics
832 9 (2009) 587–615, doi:10.1007/s10652-009-9155-2.
- 833 [27] H. Fang, J. Bai, G. He, H. Zhao, Calculations of Nonsubmerged
834 Groin Flow in a Shallow Open Channel by Large-Eddy Simulation,
835 J. Eng. Mech. 140 (2014) 04014016, doi:10.1061/(ASCE)EM.1943-
836 7889.0000711.
- 837 [28] W. van Balen, K. Blankaert, W. Uijttewaal, Analysis of the role of
838 turbulence in curved open-channel flow at different water depths by
839 means of experiments, LES and RANS, Journal of Turbulence 11 (12)
840 (2010) 1–34.
- 841 [29] C. Juez, J. Murillo, P. García-Navarro, A 2D weakly-coupled
842 and efficient numerical model for transient shallow flow and mov-
843 able bed, Advances in Water Resources 71 (2014) 93–109, doi:
844 10.1029/2018WR022982.
- 845 [30] A. Navas-Montilla, J. Murillo, Asymptotically and exactly energy bal-
846 anced augmented flux-ADER schemes with application to hyperbolic
847 conservation laws with geometric source terms, Journal of Computa-
848 tional Physics 317 (2016) 108–147, doi:10.1016/j.jcp.2016.04.047.
- 849 [31] P. Ouro, B. Fraga, N. Viti, A. Angeloudis, T. Stoesser, C. Gualtieri,
850 Instantaneous transport of a passive scalar in a turbulent separated flow,
851 Environ. Fluid Mech. 18 (2) (2018) 487–513, doi:10.1007/s10652-017-
852 9567-3.
- 853 [32] A. McCoy, G. Constantinescu, L. J. Weber, Exchange Processes in a
854 Channel with Two Vertical Emerged Obstructions, Flow, Turbulence
855 and Combustion 77 (2006) 97–126, doi:10.1007/s10494-006-9039-1.

- 856 [33] C. Gualtieri, Numerical Simulation of Flow Patterns and Mass Exchange
857 Processes in Dead Zones, in: 4th International Congress on Environmen-
858 tal Modelling and Software, Barcelona, Spain, 2008.
- 859 [34] P. Ouro, B. Fraga, U. Lopez-Novoa, T. Stoesser, Scalability of
860 an Eulerian-Lagrangian large-eddy simulation solver with hybrid
861 MPI/OpenMP parallelisation, *Computers & fluids* 179 (2019) 123–136,
862 doi:10.1016/j.compfluid.2018.10.013.
- 863 [35] Federal Office of Environment, Hydrological Data Service for water-
864 courses and lakes, URL <http://www.bafu.admin.ch/wasser>, 2016.
- 865 [36] P. Ouro, T. Stoesser, B. Fraga, U. Lopez-Novoa, Hydro3D repository,
866 doi:10.5281/zenodo.1200187, 2018.
- 867 [37] Y. Liu, T. Stoesser, H. Fang, A. Papanicolau, A. Tsakiris, Turbulent flow
868 over an array of boulders placed on a rough permeable bed, *Computers
869 and Fluids* 158 (2017) 120–132.
- 870 [38] P. Ouro, C. A. M. E. Wilson, P. Evans, A. Angeloudis, Large-eddy
871 simulation of shallow turbulent wakes behind a conical island, *Phys.
872 Fluids* 29 (12) (2017) 126601, ISSN 1070-6631, doi:10.1063/1.5004028.
- 873 [39] T. Stoesser, Physically Realistic Roughness Closure Scheme to Simulate
874 Turbulent Channel Flow over Rough Beds within the Framework of LES,
875 *J. Hydraul. Eng.* 136 (2010) 812–819, doi:10.1061/(ASCE)HY.1943-
876 7900.0000236.
- 877 [40] T. Stoesser, C. Braun, M. García-Villalba, W. Rodi, Turbulence
878 Structures in Flow over Two-Dimensional Dunes, *J. Hydraul. Eng.*
879 134 (1) (2008) 42–55, ISSN 0733-9429, doi:10.1061/(ASCE)0733-
880 9429(2008)134:1(42).
- 881 [41] W. Rodi, G. Constantinescu, T. Stoesser, Large-Eddy Simulation in
882 Hydraulics, CRC Press, ISBN 978-0-203-79757-0, 2013.
- 883 [42] S. Bomminayuni, T. Stoesser, Turbulence Statistics in an Open-Channel
884 Flow over a Rough Bed, *Journal of Hydraulic Engineering* 137 (11)
885 (2011) 1347–1358.

- 886 [43] M. Cevheri, R. McSherry, T. Stoesser, A local mesh refinement approach
887 for large-eddy simulations of turbulent flows, *International Journal for*
888 *Numerical Methods in Fluids* 82 (2016) 261–285.
- 889 [44] F. Nicoud, F. Ducros, Subgrid-scale stress modelling based on the square
890 of the velocity gradient tensor, *Flow, turbulence and Combustion* 62
891 (1999) 183–200, doi:10.1023/A:1009995426001.
- 892 [45] M. Koken, G. Constanstinescu, An investigation of the dynamics of co-
893 herent structures in a turbulent channel flow with a vertical sidewall ob-
894 struction, *Physics of Fluids* 21 (8) (2009) 085104, doi:10.1063/1.3207859.
- 895 [46] T. Meile, J.-L. Boillat, A. J. Schleiss, Flow Resistance Caused by Large-
896 Scale Bank Roughness in a Channel, *Journal of Hydraulic Engineering*
897 137 (12) (2011) 1588–1597, doi:10.1061/(ASCE)HY.1943-7900.0000469.
- 898 [47] B. A. Tuna, E. Tinar, D. Rockwell, Shallow flow past a cavity: globally
899 coupled oscillations as a function of depth, *Experiments in Fluids* 54
900 (2013) 1586, doi:10.1007/s00348-013-1586-3.
- 901 [48] M. Sanjou, I. Nezu, Hydrodynamic characteristics and related mass-
902 transfer properties in open-channel flows with rectangular embay-
903 ment zone, *Environmental Fluid Mechanics* 13 (2013) 527–555, doi:
904 10.1007/s10652-013-9279-2.
- 905 [49] C. J. Kähler, S. Scharnowski, C. Cierpka, On the uncertainty of digital
906 PIV and PTV near walls, *Experiments in Fluids* 52 (6) (2012) 1641–
907 1656, ISSN 1432-1114, doi:10.1007/s00348-012-1307-3.
- 908 [50] E. Mignot, W. Cai, G. Launay, N. Riviere, C. Escauriaza, Coherent tur-
909 bulent structures at the mixing-interface of a square open-channel lateral
910 cavity, *Physics of Fluids* 25 (2016) 045104, doi:10.1063/1.4945264.
- 911 [51] D. Rockwell, C. Knisely, Observations of the three-dimensional nature
912 of unstable flow past a cavity, *Physics of fluids* 23 (1980) 425, doi:
913 10.1063/1.863009.
- 914 [52] M. Wölfinger, C. A. Ozen, D. Rockwell, Shallow flow past a cavity: Cou-
915 pling with a standing gravity wave, *Physics of fluids* 24 (2012) 104103,
916 doi:10.1063/1.4761829.

- 917 [53] V. Nikora, R. Nokes, W. Veale, M. Davidson, G. H. Jirka, Large-scale
918 turbulent structure of uniform shallow free-surface flows, *Environmental*
919 *Fluid Mechanics* 7 (2007) 159–172, doi:0.1007/s10652-007-9021-z.
- 920 [54] J. Sommeria, Experimental study of the two-dimensional inverse energy
921 cascade in a square box, *Journal of Fluid Mechanics* 170 (1986) 139–168,
922 doi:10.1017/S0022112086000836.
- 923 [55] V. Nikora, Origin of the "21" Spectral Law in Wall-Bounded
924 Turbulence, *Physical Review Letters* 83 (1999) 734, doi:
925 10.1103/PhysRevLett.83.734.
- 926 [56] R. Kraichnan, Inertial Ranges in Two-Dimensional Turbulence, *Physics*
927 *of Fluids* 10 (1967) 1417, doi:10.1017/S0022112086000836.